

Spontaneous Optimal Mixing via Defect-Vortex Coupling in Confined Active Nematics

Brandon Klein,¹ Alejandro J. Soto Franco,^{1,2} Md Mainul Hasan Sabbir,³ Matthew J. Deutsch,⁴ Ross Kriegman,¹ Robin L. B. Selinger,^{4,5} Kevin A. Mitchell,³ and Daniel A. Beller^{1,*}

¹*Department of Physics and Astronomy, Johns Hopkins University, Baltimore, Maryland 21218, USA*

²*Department of Biomedical Engineering, Johns Hopkins University, Baltimore, Maryland 21218, USA*

³*Department of Physics, University of California, Merced, California 95344, USA*

⁴*Advanced Materials and Liquid Crystal Institute, Kent State University, Kent, Ohio 44242, USA*

⁵*Physics Department, Kent State University, Kent, Ohio 44242, USA*

(Dated: April 29, 2025)

Active nematic flows in two dimensions, largely driven by motile $+1/2$ disclinations, mix themselves efficiently and exhibit chaos in the bulk steady state. Motivated by recent experimental findings for three-defect braiding in cardioid-shaped domains, we investigate how this tendency toward chaotic fluid mixing can, counterintuitively, produce certain ordered, periodic flows in confinement with a controllable net topological charge. We study two-dimensional active nematics in systems with boundary conditions requiring a prescribed number of excess $+1/2$ disclinations, using Beris-Edwards nematohydrodynamics simulations, alongside an agent-based, hydrodynamic simulation approach. We find ordered flows for systems of three and four defects, and we use tools from braid theory to show that spontaneously occurring periodic defect motions produce maximal topological entropy. Our theory correctly predicts the generic absence of stable periodic orbits of more than four defects in strong confinement in simulation. Our results identify the parameter regime outside of which periodicity is lost, and allow us to probe the limits of topological entropy production.

I. INTRODUCTION

Active systems, like all life, are far from equilibrium, generating work from energy sources in their surroundings. This non-equilibrium driving prevents the stability of ordered ground states. Strikingly, topological defects have been found to play important and diverse roles in the dynamics of many active systems, both natural and synthetic, especially in the form of disclination defects in nematic director fields [1–7]. This has inspired much interest in describing and controlling defects and their dynamics for fundamental understanding and for possible microfluidic and industrial applications. To these ends, model active nematic systems have been constructed *in vitro* from biological components. One common method [8, 9] involves microtubule bundles suspended in a fluid with ATP-powered kinesin dimers, which walk along the microtubules, pushing them in opposite directions and thereby injecting extensile activity into the system. With model systems such as these, much has been learned about defect control [10–13] and ordered flows [14, 15].

Bulk active nematics are known to exhibit chaotic defect motion [16], and much work has been done in creating control mechanisms for their flow structures and dynamics to tame this chaos. For example, Gaussian curvature tends to charge separate topological defects with the same sign [17], substrate friction has been shown to tune the characteristic length scales of director distortions in active nematics [18], and topographical patterns in the substrates underlying nematic fluids exhibit remarkable

control over the rheological properties of the bulk [19]. The realm of defect spatiotemporal control has also been explored using activity gradients as effective electric fields for defect quasi-particles [20, 21], and has been achieved experimentally with light activation of myosin molecular motors [22].

One vital control mechanism for nematic flow structures is that of boundary conditions and the constraints they impose on bulk systems. For example, when active nematics are confined to a disk [23], an ordered state is produced in which two positive $+1/2$ defects circle around a common vortex core, periodically interrupted by $\pm 1/2$ defect pair nucleation and pair annihilation. In simulations of annuli and disks with variable winding number, defects have a tendency to self-screen excess topological charge [24, 25] by localizing near boundaries. This effect is prominent when active nematics are confined to a channel, where they can produce an array of vortices around which defects rotate in an alternating “dance” [26]. The negative defects pin to the walls of the channel allowing for the smooth motion of $+1/2$ defects without annihilation. When periodic obstacles are placed through the nematic bulk, a 2D vortex lattice can be stabilized [27]. Both of these systems take place on periodic boundaries. It was recently shown that a periodic 2D plane alone can produce an ordered braiding motion of $+1/2$ defects around quasi-stationary negative defects [28]. This braiding motion was shown to be identical to the braid conjectured, with strong numerical evidence, to be the maximally mixing braid on a topological annulus as measured by *topological entropy* [29].

Recently, Memarian and coauthors [30] showed that a cardioid-like boundary can pin a negative defect at the inward-facing cusp, allowing three motile positive defects

* d.a.beller@jhu.edu

to encircle each other in alternating swaps, in a pattern known as the golden braid. This braid is proven to be the optimal mixing braid for three “stirring rods” [31].

These findings highlight a need for more general understanding of how topological defect dynamics in active nematics respond to the geometry and topology of confining boundaries. In this work, we investigate governing principles responsible for the golden braid in confined active nematics with three $+1/2$ defects, and whether similar periodic orbits can be obtained with other numbers of motile defects. We present a novel application of braid theory and topological entropy, alongside numerical modeling of extensile active nematic dynamics, to predict emergent flow patterns. We demonstrate commonalities in defect braiding dynamics between the experimentally relevant scenario of curved boundaries with tangential anchoring and a theoretical construct of circular boundaries with spatially varying anchoring, whose winding encodes the net topological charge. Our modeling captures and rationalizes previous observations for two and three defects, identifies a new ordered state for four defects, and predicts an absence of periodic braiding for five or more defects. We corroborate our simulated Beris-Edwards nematohydrodynamics with a new, agent-based model of active nematic filaments coupled to a coarse-grained fluid. We propose a topological connection between defect braiding and vortex structure in the fluid velocity field, offering an explanation for the limited scenarios that permit periodic defect braiding and predicting bounds on topological entropy production.

II. METHODS

A. Beris-Edwards nematohydrodynamics

We computationally model an extensile active nematic in two dimensions, with nematic order represented by the second-rank tensor

$$Q_{ij}(\mathbf{r}) = S(\mathbf{r}) \left(n_i(\mathbf{r})n_j(\mathbf{r}) - \frac{\delta_{ij}}{2} \right), \quad (1)$$

where \mathbf{n} is the director, δ_{ij} is the Kronecker delta, i and j run over two dimensions, and S is the scalar degree of nematic order.

We simulate Beris-Edwards nematohydrodynamics [32] in a finite difference scheme on a square lattice, similarly to the approach of Ref. [33], describing the coupled evolution of the nematic order, Q_{ij} , and the flow field, \mathbf{u} . The time-evolution of Q_{ij} is governed by

$$\begin{aligned} \partial_t Q_{ij} + u_k \partial_k Q_{ij} = \\ \frac{1}{\gamma} H_{ij} + \chi S E_{ij} + [Q, \omega]_{ij} - 2 \text{Tr}[QE] Q_{ij}. \end{aligned} \quad (2)$$

Here, $[\cdot, \cdot]$ is the commutator, \mathbf{u} is the flow field, γ is the rotational viscosity, χ is a flow aligning or tumbling parameter, and $E_{ij} = (\partial_i u_j + \partial_j u_i)/2$ and $\omega_{ij} =$

$(\partial_i u_j - \partial_j u_i)/2$ are the rate-of-strain and vorticity tensors respectively. H_{ij} is the molecular tensor associated with the Landau-de Gennes free energy

$$\begin{aligned} F_{\text{LdG}} = \int_{\Omega} \left[\frac{A}{2} \text{Tr}[Q^2] \left(1 - \frac{1}{2} \text{Tr}[Q^2] \right) \right. \\ \left. + \frac{K}{2} (\nabla_i Q_{jk})(\nabla_i Q_{jk}) \right] d\Omega, \end{aligned} \quad (3)$$

$$\begin{aligned} H_{ij} = - \frac{\delta F_{\text{LdG}}}{\delta Q_{ij}} \\ = -Q_{ij} A (1 - \text{Tr}[Q^2]) + K \nabla^2 Q_{ij}. \end{aligned} \quad (4)$$

Here, $A < 0$ and sets the energy cost of a defect, K is the Frank elastic constant in the one-constant approximation, and Ω is the nematic domain.

The time evolution of \mathbf{u} is given by the incompressible Navier-Stokes equations,

$$\partial_t \mathbf{u} + (\mathbf{u} \cdot \nabla) \mathbf{u} = \eta \nabla^2 \mathbf{u} + \frac{1}{\rho} \mathbf{F} - \frac{1}{\rho} \nabla p, \quad (5)$$

$$\nabla \cdot \mathbf{u} = 0, \quad (6)$$

where η is the fluid viscosity, ρ is the (constant) density, and the force density \mathbf{F} is the divergence of a stress tensor Π_{ij} :

$$\begin{aligned} F_i = \partial_j \Pi_{ij} = \partial_j [-H_{ij} - \zeta Q_{ij} + [Q, H]_{ij}] \\ + 2 \text{Tr}[QH] Q_{ij} - K \partial_i Q_{kl} \partial_j Q_{kl}. \end{aligned} \quad (7)$$

Here, ζ is the activity, coupling the flow field time evolution to nematic stresses. For all systems considered here, $\zeta > 0$, which corresponds to extensile activity.

This scheme, when simulated in periodic boundaries, reproduces the well-known bulk behavior of “topological chaos” [16, 33–35], generating $\pm 1/2$ topological defects corresponding to locally melted regions of the nematic order which couple to the surrounding flow field. There are two characteristic length scales that emerge from these equations of motion: the active length scale $\ell_a = \sqrt{K/\zeta}$ which scales with the average defect spacing, and the nematic coherence length $\ell_c = \sqrt{K/|A|}$ which scales with the average defect core radius. These length scales will be varied to explore the regime of active steady states. Thus, providing a non-dimensional description of them will be of use. To do this, we normalize them by the effective system length, given by the square root of the system area in units of lattice spaces. For each studied geometry, we tune the activity within a range such that $+1/2$ defects are motile and fixed in number, with total topological charge q determined by the geometry. The activity is kept low enough to prevent spontaneous defect pair production, as the regime of active turbulence is not the focus of this study. We use the following values throughout: $\rho = 1$, $\chi = 1$, $K = 2^{14}$, $\gamma = 100$, and $\eta = \sqrt{10 \cdot 2^{14}}$.

For simplicity, we take anchoring at the boundaries to be infinitely strong, creating Dirichlet boundary conditions on Q . For the velocity field, a no-slip condition $\mathbf{u} = \mathbf{0}$ is applied at the boundaries.

More details are given in Appendix A 1.

B. Fluid mixing and defect braiding

Tan and coauthors [16] showed that the fluid mixing capabilities of active nematics are deducible from the braiding motions of the worldlines of $+1/2$ topological defects. The self propulsion of the $+1/2$ defects drives the dynamic evolution of the Lagrangian coherent structures which connect initially infinitesimally close passive tracers in the bulk, and is thus correlated to the production of a positive Lyapunov exponent (Figure 1b). By viewing $+1/2$ defects as self-propelled stirring rods, we can measure the amount of stretching their dynamics inject into the bulk and quantitatively distinguish dynamic patterns by their fluid mixing capability.

We can describe this stretching by considering an infinitely elastic boundary enclosing the defects, which stretches as the defects or stirring rods stretch the initial boundary over time. A lower bound on this stretching, corresponding to pulling the boundary line taught around the defect cores, is given by an exponential function of time from an initial length L_0 :

$$L(t) = L_0 e^{ht}. \quad (8)$$

Here, the exponential rate of stretching h is known as the *topological entropy* (Figure 1c). This scheme for viewing topological defect dynamics is useful for several reasons. Firstly, the topological entropy is an upper bound on the Lyapunov exponent [36] (Figure 1b), and in experiments on microtubule-based active nematics, this bound is nearly met. Secondly, it is possible to analytically calculate topological entropy in periodic flows. Hence, we can use h as a proxy for λ , and measure the chaotic character of active nematics by measuring the stretching injected into the bulk fluid.

Analytical calculation of h relies on the description of worldlines of n positive defects within the Artin Braid group \mathbf{B}_n [37]. The relationship between braiding of defect worldlines and fluid mixing that we calculate assumes that the positive defects act as stirring rods, meaning that their velocity is equal to the local fluid velocity as would be the case if they were solid objects [16]. At any instant, we order the $+1/2$ defects by projecting their 2D positions onto a line, which we take to be the x axis but which can be oriented in an arbitrary direction.

As time progresses, changes in this ordering of projected defect positions take place through swaps between defects with consecutive indices i and $i + 1$ in the ordering. Each such inversion corresponds to one of two *braid generators*, σ_i or σ_i^{-1} , depending on whether it occurs in a clockwise (CW) or counter-clockwise motion (CCW) respectively; in the projection, these two cases

correspond to defect i passing behind or in front of defect $i + 1$. Thus, for n defects, a set of $2(n - 1)$ generators completely describes the set of inversions that can occur, and their products can describe all possible dynamics, an example of which can be seen in Figure 1d. A *braidword*, β , is a sequence of braid generators.

The braid generators can be given in the Burau representation (see Appendix B) as $(n - 1) \times (n - 1)$ matrices

$$\begin{aligned} (\sigma_i)_{kl} &= \delta_{kl} + \delta_{i-1,k} \delta_{il} - \delta_{i+1,k} \delta_{il}, \\ (\sigma_i^{-1})_{kl} &= \delta_{kl} - \delta_{i-1,k} \delta_{il} + \delta_{i+1,k} \delta_{il}. \end{aligned} \quad (9)$$

This matrix representation is constructed to maintain the Artin group relations: $[\sigma_i, \sigma_j] = 0$ if $|i - j| > 1$, and $\sigma_i \sigma_{i+1} \sigma_i = \sigma_{i+1} \sigma_i \sigma_{i+1}$. Importantly, this means that a braidword can be represented as a matrix product, and that a periodic steady state corresponds to the application of β^{n_c} for n_c cycles. In the large- n_c limit, the matrix product β^{n_c} in its eigenbasis is dominated by its largest-magnitude eigenvalue $b_{\max}^{n_c}$, where b_{\max} is the largest eigenvalue of β . Because the defects, as stirring rods, drag the fluid with them, the minimal stretching of material contours required to accommodate the described defect braiding grows with n_c as $b_{\max}^{n_c}$. The topological entropy therefore grows linearly with n_c , as $h = \log(|b_{\max}^{n_c}|) = n_c \log(|b_{\max}|)$. Since n_c is proportional to time for periodic braiding, the slope of $h(t)$ is proportional to $\log(|b_{\max}|)$. Note that, if the motion is periodic, h is independent of the projection used.

We numerically compute the topological entropy for the two-dimensional active flow by two schemes using the flow field. In the first method, known as the *Line Stretching* algorithm, we advect an initial line segment forward in time according to the local flow, and track the length of the newly advected contour. If the advected segment grows exponentially in time, then the slope from the semi-log plots of contour length over time yields the topological entropy (Supplemental Videos 2 and 3). Secondly, we use a computational geometry-based algorithm, known as the *E-tec* (Ensemble-based topological entropy calculation) method [38]. We advect an ensemble of randomly initialized passive tracers forward in time. The E-tec algorithm computes a lower bound on the entire system's topological entropy using the finite trajectories of the random ensemble. Full details are provided in Ref. [38]. To compute the Lyapunov exponent, we randomly choose a pair of passive tracers with a very small initial separation distance and track how their separation distance evolves in time. This method quantifies the largest Lyapunov exponent as it only measures the maximum stretching of two nearby tracers without any restriction on the direction of the stretching.

III. RESULTS

A. Circular confinement with controllable topological charge

To systematically tune the number of mobile $+1/2$ defects, we consider circular confinement of the active nematic phase while varying the anchoring direction of the nematic director on the boundary so as to require a net enclosed topological charge of q . In particular, with the circular boundary $\partial\Omega$ parameterized by angle θ , we initialize the nematic order as

$$\mathbf{n}|_{\partial\Omega}(\theta) = \pm \begin{pmatrix} -\sin(q\theta) \\ \cos(q\theta) \end{pmatrix}, \quad (10)$$

and set the scalar degree of order, S , to $\sqrt{2}$. The Q -tensor defined by Equations 1 and 10 is held fixed at the boundaries. This boundary condition produces a net topological charge q in the nematic domain Ω , causing the lowest-energy states to have $n = 2q$ topological defects with winding number $+1/2$.

We first consider a circular boundary with tangential anchoring, providing a net charge of $q = +1$, thus requiring two $+1/2$ topological defects. This system was realized by Ref. [23] and, similarly, we find that the two positive defects circle a common direction, creating the braidword $\{\sigma_1^{\pm 1}\}$ and zero topological entropy, as shown in Figure 2 and Supplemental Video 1. In the experimental system of Ref. [23], the co-rotating defects deviate from their quasi-circular trajectories upon the nucleation of a defect pair from the boundary, whose negative defect annihilates one of the bulk defects. Beris-Edwards nematic hydrodynamics, however, do not observe such breaking of periodicity below the activity threshold to active turbulence [39–41]. Likewise, we find that the co-rotating defects are an active steady state. The only braidwords that can be created in \mathbf{B}_2 (i.e., with two defects) are $\{\sigma_1^{\pm 1}\}$ and the identity, which both have a maximum eigenvalue of 1. This is consistent with the fact that two stirring rods are incapable of producing chaotic mixing [36].

For $q = 3/2$, we observe that the three $+1/2$ defects spontaneously produce the “golden braid” observed in cardioid-shaped confinement in Ref. [30]. Consecutive inversion events in the golden braid alternate between CW and CCW, and the same two defects are never swapped before one of them is swapped with the third. Traces of the defect trajectories, along with the worldlines of their x -projections, are shown in the top row of Fig. 3a,b and in Supplemental Video 2. The golden braid is described by the braidword $\{\sigma_1\sigma_2^{-1}\}$, which yields a topological entropy of $h = 2 \log \phi_0$, where $\phi_0 = (1 + \sqrt{5})/2$ is the golden ratio, for which the golden braid is named [37]. We normalize this by the number of swaps, two in this case, where a swap corresponds to a co-linear arrangement of defects throughout the trajectory. This prediction agrees well with the topological entropy as numerically calcu-

lated using both the Line Stretching and E-tec schemes (Fig. 3c).

The boundary condition producing $q = 4/2$ results in a periodic active steady state of four $+1/2$ defects, which to our knowledge has not previously been studied in an active nematic. Defect trajectories and projection worldlines are shown in the bottom row of Fig. 3a, b and in Supplementary Video 3. The braidword for this motion is $\{\sigma_1\sigma_3\sigma_2\sigma_1^{-1}\sigma_3^{-1}\sigma_2^{-1}\}$. Because the associated topological entropy is $h = 2 \log(\phi_1)$, where $\phi_1 = 1 + \sqrt{2}$ is the silver ratio, this braid is known as the “silver braid” [37]. Unlike the $q = 3/2$ case, here the $+1/2$ do not all follow the same trajectory; instead, there are two intersecting, mirror-image trajectories, each containing two of the four defects. This braid is topologically equivalent to the “Ceilidh dance” [26] with four $+1/2$ defects, with the distinction that the topology of our system is a disk, not an annulus, and therefore lacks the pinned negative defects seen in annular confinement. Since all four defects are co-linear twice throughout the trajectory of this braid, we normalize the topological entropy by two swaps.

In contrast to the systems of two, three, and four defects, we find that boundary conditions with q between $5/2$ and $10/2$ do not spontaneously adopt periodic motions of their five to ten $+1/2$ defects, as seen in 4a. The ground states for a passive nematic in the same geometries are shown in Fig. 4b, revealing n -fold rotational symmetry in the equilibrium locations of $n + 1/2$ defects close to the boundary. Across all studied active length scales ℓ_a and nematic coherence lengths ℓ_c , these systems do not exhibit a periodic motion of defects as their active steady state. We do observe a brief time-regime in which the defects appear to follow regular braids generalizing the structures observed for lower $n = 2q$, with braidword given by

$$\{\sigma_n\sigma_{n-2}\dots\sigma_{n-1}\sigma_{n-3}\dots\sigma_n^{-1}\sigma_{n-2}^{-1}\dots\sigma_{n-1}^{-1}\sigma_{n-3}^{-1}\dots\}. \quad (11)$$

With $n = 4$, this braidword describes the observed silver braid for $q = 4/2$. For large q , Eq. 11 gives a topological entropy of $h \approx 2.88$. However, for $n \geq 5$, the predicted braid is replaced by apparently random motions partway through the braidword.

Despite the lack of periodic braiding in $n \geq 5$ defects, we observe a great deal of structure in the time-averaged vorticity, plotted in Fig. 4c. We will focus on the $n = 5$ defect case when discussing unstable systems for the rest of this work, as our understanding of the instability of higher charge cases applies to all $n \geq 5$ systems.

It is interesting to note that ℓ_a has to be decreased as q increases in order for the defects to remain mobile. As seen in Fig. 4a, some defects in the $q = 9/2$ and $q = 10/2$ systems remain close to their passive ground-state positions throughout the simulation. This is consistent with previous work showing that defects screen boundary charge [24], with the distinction that here we observe this effect in *positively-charged* defects.

B. Boundary-imposed forces

To understand the emergence of the observed defect braids for $n \leq 4$, as well as the generalizability of the dynamics they realize, we examine the relationship between defect trajectories and the forces and torques imposed by the boundary conditions. We observe that the tangent to a defect trajectory at a given point tends, when possible, to be parallel to a straight line drawn through some point on the boundary and oriented along the director there. From Eq. 10, these lines are given by

$$f(u) = (y - r \sin(u)) + \cot(qu)(x - r \cos(u)) = 0, \quad u \in [0, 2\pi]. \quad (12)$$

Here, r is the radius of the circular confinement. This alignment can be understood geometrically as a dynamically stable situation for a self-propelling $+1/2$ defect. Since the defect experiences an active force in the direction of its comet-head, its tail is the only side that can be stably aligned with a fixed director at the boundary. This idea is illustrated in Figure 5a, where defects with three distinct orientations are drawn along with a line on which the director is imagined to be held fixed parallel to the line. The only defect that is aligned with the fixed director more than instantaneously is the one whose self-propulsion lies along the line. If we now consider the family of lines defined by Eq. 12 (Fig. 5b), the scheme of orienting defects parallel to these lines results in a dynamic stability for points in the interior region, whereas for certain regions near the boundary, many possible trajectories converge, pushing defects into the interior region.

The boundary between these two types of regions is the envelope of the family of lines, which is tangent at each point to one such line. The unique solution for this envelope satisfying $f(u) = \partial_u f(u) = 0$ is given by

$$\begin{aligned} x(u) &= \frac{r}{2q}[(2q-1)\cos(u) + \cos((2q-1)u)] \\ y(u) &= \frac{r}{2q}[(2q-1)\sin(u) + \sin((2q-1)u)], \quad u \in [0, 2\pi]. \end{aligned} \quad (13)$$

These are the equations defining an epicycloid [42]. Geometrically, epicycloids are constructed by tracing the path of a point on a circle of radius r_c as it rolls on the circumference of a circle r . In this construction, $r/r_c = 2(q-1) = n - 2$, which is the number of cusps in the resulting closed curve. For $q = 3/2, 4/2$ and $5/2$, the envelopes are called a cardioid, a nephroid, and a trefoiloid respectively [42].

We observe that these epicycloid envelopes predict certain important features of the simulated defect trajectories, as shown in Figure 5c. Defect trajectories remain approximately inside the envelopes. Furthermore, over certain regions beginning near a cusp in an envelope and ending at that cusp, the defect trajectories approximately coincide with the envelope while undergoing large-angle

reorientation. We can understand how active forces yield this relationship by identifying

$$\mathbf{F}_{\text{active}}|_{\partial\Omega} = -\zeta \nabla \cdot \mathbf{Q}|_{\partial\Omega} = \frac{S\zeta q}{|\mathbf{r}|} \begin{pmatrix} \cos((2q-1)\theta) \\ \sin((2q-1)\theta) \end{pmatrix}. \quad (14)$$

It is useful to compare the right-hand side of Eq. 14 to $\mathbf{F}_{\text{active}} = S\zeta(\mathbf{S} - \mathbf{B})$ where $\mathbf{S} = \mathbf{n}(\nabla \cdot \mathbf{n})$ is the splay vector and $\mathbf{B} = \mathbf{n} \times (\nabla \times \mathbf{n})$ is the bend vector. The bend contribution along the boundary has squared magnitude

$$|\mathbf{B}|^2 = \frac{1}{S^2\zeta^2} |\mathbf{n} \cdot \mathbf{F}_{\text{active}}|^2 = \frac{q^2}{r^2} \sin^2((q-1)\theta),$$

which is maximal at places where the anchoring is tangential, and the splay contribution has squared magnitude

$$|\mathbf{S}|^2 = \frac{1}{S^2\zeta^2} |\mathbf{n} \times \mathbf{F}_{\text{active}}|^2 = \frac{q^2}{r^2} \cos^2((q-1)\theta),$$

which is maximal at places where the anchoring is radial. We find that the defects tend to move along tangentially anchored boundaries, where the bend mode dominates the active force, until the defect reaches the next radially-anchored location where the splay mode of the active force reorients the defect trajectory into the bulk. These splay maxima occur at the θ -value of a cusp in the envelope curve, as each cusp lies along a line connecting the center of the system to a boundary point where the anchoring points radially along that line. Thus, defects experience maximum boundary-imposed splay at the envelope cusps, pushing the defects toward the center as we observe.

The utility of the epicycloid envelopes is then two-fold: they can predict all of the locations of sharp reorientation events in the defect trajectories, and (consequently) they approximate an effective boundary for the region of observed defect motions. These control mechanisms hold both for the time-periodic ($n \leq 4$) systems and the non-periodic ($n \geq 5$) systems; hence, we can use them to understand the defect braiding dynamics that they permit or prohibit.

C. Flow-field structure

Nematic hydrodynamics produces a two-way coupling between the structure of the flow velocity field \mathbf{u} and the director field \mathbf{n} , and we see this reflected in the coupled topologies of the two fields. In addition to determining the reorientation sites of defect trajectories, the active force encoded by the boundary conditions acts on the flow field. Thus, understanding how the structure of the flow field is mutually-consistent with the boundary-imposed active force will be useful for characterizing the general dynamics of $n = 2q$ positive defects with anchoring of winding q . Here, by fixing the director at the boundary with nontrivial winding, we set up patterns of

active force by which we can sculpt the dominant flow structures within the bulk.

To elucidate the coupling of the director and velocity fields, we examine the instantaneous and time-averaged vorticity of the flow structures underlying the observed braiding dynamics. We define the boundaries of vortices using the second invariant of the velocity gradient tensor, known as the \mathcal{Q} -criterion [43]:

$$\mathcal{Q} = \frac{||\omega||^2 - ||E||^2}{2}. \quad (15)$$

Positive values of \mathcal{Q} correspond to vorticity-dominated regions and negative ones to strain-dominated regions. Thus, the closed isolines of $\mathcal{Q} = 0$ provide well-defined vortex boundaries.

Defect motions and vortex structure are strongly linked through the \mathcal{Q} -criterion: the trajectories of $+1/2$ defects in simulated and experimental active nematics data closely follow isolines of $\mathcal{Q} = 0$, an observation rationalized by the fact that the Stokes-flow solution for an isolated $+1/2$ defect lies on a $\mathcal{Q} = 0$ isoline [43]. We observe this “self-constraint” between the \mathbf{n} and \mathbf{u} fields to be well-obeyed in our system, for both periodic and aperiodic motion as exemplified by the snapshots in Figure 6a. The instantaneous and running time-averaged fields of both ω and \mathcal{Q} , along with their standard deviations, are shown for the $q = 3/2, 4/2$, and $5/2$ systems in Supplemental Videos 4, 5, and 6.

Importantly, we find that the swapping of defects necessitates a topological change of $\mathcal{Q} = 0$ isolines: Because each $+1/2$ defect is always at a location with $\mathcal{Q} = 0$ instantaneously, and the $\mathcal{Q} = 0$ subset consists of closed curves each surrounding a vortex ($\mathcal{Q} > 0$), a defect can only move from one vortex to another by instantaneous intersection of two $\mathcal{Q} = 0$ loops into a “figure eight”. These intersections are visible in some of the snapshots of Fig. 6a. In order for the circulation direction of the vortex to be consistent with the $+1/2$ defect’s heading, these direct vortex-swapping events only take place between vortices of opposite-sign vorticity.

However, defects can also swap with one another between same-sign vortices by a more complicated choreography, seen in the $q = 4/2$ system (Fig. 6a middle row): Two CW vortices merge into one, while coming temporarily into contact with the two CCW vortices. Two defects, previously on the two separate CW vortices, are now pinned to these two $\mathcal{Q} = 0$ junctions while continuing to circulate clockwise. Then, the CW vortex splits again into two while breaking contact with the CCW vortices. The flow field has now returned to its original structure, but with two defects having swapped CCW vortices. The mirror-image process then occurs to allow swapping of the other two defects between the two CCW vortices. These alternating swaps produce the two distinct, overlapping defect trajectories in Fig. 5c.

The time-averaged vorticity for these three systems, plotted in Fig. 6b, is markedly dominated by $4(q-1)$ alternating gyres of opposite vorticity. The time-averaged

behavior dominates the instantaneous dynamics, in the sense that we measure a small noise-to-signal ratio, defined as the spatially averaged ratio between the standard deviation and the time average of the vorticity over all lattice points. These ratios are 0.1048 for the $3/2$ system, 0.0069 for the $4/2$ system and 0.0007 for the $5/2$ system.

Gyre boundaries divide adjacent regions of alternating time-averaged vorticity, partitioning the domain. Each gyre boundary advects material either toward or away from the fluid boundary layer, where the vorticity changes sign to accommodate the no-slip boundary condition [33, 44]. (For $q = 3/2$, the single gyre boundary moves material away from one side of the circle and toward the other.) The locations where gyre boundaries advect material away from the boundary coincide with the angular positions of the cusps in the envelope curves plotted in Fig. 5b. Equivalently, this means that the lobes between cusps on the envelope also each contain two counter-rotating domains but in such a way that the flow advects material along the boundary. This matches our findings that splay deformation fixed by the boundary condition scatters defects into the bulk while fixed bend polarization allows them to travel along the boundary. The cusps thus behave similarly to “wall defects” observed in experiment to arise spontaneously in active nematics confined to a disk [25].

The global consistency of these dynamics can be understood schematically as a directed graph over each envelope, as shown in Fig. 6c. Each node corresponds to either a cusp or a bulge, and directed edges signify the local flow direction such that the gyre structure is summarized by cycles in the graph. Importantly, the net degree of every node is 0, representing the incompressibility constraint. This yields a unique gyre structure for every q , in good agreement with that measured in Fig. 6b.

To find a general expression for the number of gyres, we can count the sectors of the active force field at the boundaries as the number of times the active force vector is aligned parallel or antiparallel to \hat{r} as we vary over orientations in the plane. Thus, the number of gyres is given by the number of solutions to

$$\mathbf{r} \times \mathbf{F}_{\text{active}} = S\zeta q \sin(2(q-1)\theta) = 0, \quad (16)$$

from which we find that the number of gyres grows as $4|q-1|$, as we observe numerically (Fig. 6b). In contrast, the number of defects grows as $2q$. This leads to the simple but important observation that for $q > 4/2$, there are more gyres than defects. While there may be time-variation in the number of vortices, the active force field required by the boundary conditions demands that the number and structure of vortices give, on average, the gyre structures of Fig. 6b. As seen in Fig. 6a and Supplemental Video 6, vortices without defects are unstable and tend to decay in size; some disappear entirely, to be replaced by nucleation of a new $\mathcal{Q} = 0$ loop elsewhere in the system. This instability is consistent with the previously observed enhancement of vortex stability by the presence of a $+1/2$ defect [33, 43].

The presence or absence of such defect-free vortex “holes” is important to defect braiding because $+1/2$ defects tend to distribute themselves evenly among the available $Q = 0$ loops (presumably due, at least in part, to elastic repulsion between like-sign defects) so a hole will be available for a defect to transfer to only if the vortices outnumber the defects. Otherwise, a defect can only transfer to another $Q = 0$ loop by a coordinated swap with another defect. Sequences of these pairwise swaps are required for periodic braiding and maximal topological entropy production, which thus occurs only for $q = 3/2$ and $4/2$.

Understanding of this complex interplay of flow-field and director topologies is facilitated by a schematic representation of defect paths consistent with the time-averaged vorticity. This representation, shown in Fig. 6c, takes the form of a directed graph whose edges imply a “flow” consistent with the corresponding gyres of Fig. 6b. One node is placed for each pair of adjacent, counter-rotating gyres. A defect encountering a node can exit it along either of two outward-directed edges, one of which keeps the defect on the same gyre, while the other represents a transfer to the neighboring gyre. For $q = 3/2$ or $4/2$, such a transfer necessarily causes a temporary “overcrowding” of one gyre by two defects, leading to the transfer of the gyre’s original defect to another gyre. For $q = 3/2$, there is only one other gyre available, while for $q = 4/2$, transfer to the single empty gyre is favored, ensuring a pairwise swap of the two transferring defects.

D. Geometrically structured confinement with tangential anchoring

In order to realize the braiding patterns seen in circular confinement with variable topological winding imposed by the boundary, we require a way of modulating the mobile bulk charge in systems with strong tangential anchoring, which is the only type of anchoring currently producible in active nematics [9]. To do this, we make use of the fact that the tangent vector to the envelope curves at the cusp picks up an instantaneous rotation of $-\pi$. For the director field, strong tangential anchoring at the cusp is equivalent to replacing the cusp with a smooth arc and pinning a $-1/2$ topological defect there. Each cusp is therefore topologically balanced by an additional $+1/2$ defect in the bulk besides the two already present inside a circular boundary. Recent experiments by Memarian and coauthors [30] demonstrated exactly this approach with a microtubule-kinesin active nematic confined in a cardioid-shaped region, resembling the single-cusp, $q = 3/2$ epicycloid above. The pinning of a negative defect at the cusp resulted in a third $+1/2$ defect in the bulk, leading to an experimental realization of the golden braid dynamics. Additionally, recent theoretical work [45] predicted the same braiding dynamics in an analytical, effective-quasiparticle model of defect motion.

Here, we generalize this experimentally accessible approach to tangential-anchoring boundaries with more than one cusp, allowing control over the net topological charge, by assuming confinement geometries to be similar to the epicycloid envelope curves studied in the previous section. Specifically, to regularize the cusps of the epicycloids into \mathcal{C}^1 -continuous curves, we use as our family of boundary surfaces the *epitrochoids* defined parametrically by

$$\begin{aligned} x(u) &= \frac{r}{2q} [(2q-1) \cos(u) + d \cos((2q-1)u)] \\ y(u) &= \frac{r}{2q} [(2q-1) \sin(u) + d \sin((2q-1)u)] \quad (17) \\ u &\in [0, 2\pi], \end{aligned}$$

where $0 \leq d \leq 1$ and continuously interpolates between the epicycloids and a circle. These represent paths tracing a point on a circle of radius r at distance $r \cdot d$ from its perimeter as it rolls on the circumference of a circle R . We use $d = 0.99$ to approximate the epicycloids near their sharp limit.

In an epitrochoid with $q = 3/2$ or $4/2$, we obtain the golden and silver braids (Figure 7b) as predicted by the corresponding epicycloid envelope in the previous section. Here, this occurs through the pinning of a $-1/2$ defect to each of the (regularized) cusps as seen in 7c, leaving three or four $+1/2$ defects to interact in the bulk. The geometry of the $-1/2$ defect reorients the bulk director field nearby, creating the splay mode seen at the envelope cusp in circular confinement, and thus providing the inward active force that promotes the double or quadruple gyre flow structure. In general, we find that the pinning of negative defects changes the active force produced by the new effective boundary and realizes the same topology of active force structure described in equation 14 in circular confinement, and thus the same number of gyres.

Interestingly, this system exhibits a strongly metastable regime, shown in Supplementary Videos 7 and 8, in which one or two defects are absorbed into a cusp and then emitted during part of the braid cycle. Within the braiding taxonomy this is simply rectified by permitting that the braid strands can jump from the absorbed defect to the corresponding new positive charge once it nucleates from the cusp into the bulk (Fig. 7a).

E. Agent-based active nematic filament simulations

To assess the generality of the theory, we note the importance of density fluctuations in active microtubule experiments which are absent in the Beris-Edwards model. We simulate a three-dimensional system of active microtubules confined in a thin layer vertically and in a cardioid geometry laterally, using an agent-based, coarse-grained model of active bead-spring filaments as described in Appendix A 2. A small thickness, L , in the

third dimension allows filament cross-over and is crucial for reproducing defect dynamics. Uniquely, the active filaments are coupled to a two-dimensional underlying coarse-grained fluid layer. This fluid layer provides two important properties otherwise missing from the coarse-grained active model: long-range hydrodynamic interactions and a momentum-conserving thermostat. The hydrodynamic interactions permit similar density fluctuations to microtubule experiments. Temperature control was achieved using a pairwise dissipative particle dynamics thermostat and was passed through to the active layer of the simulation via an active-fluid particle interaction moderated by an artificial distance offset.

Our agent-based model closely mimics experimental realizations of strongly confined microtubule-kinesin active nematics [15, 23]. Simulations consist of 64,000 active particles comprising 800 filaments, each with 80 beads, and an additional 3068 fluid particles. The time evolution of these active filaments is shown in Figure 8a and in Supplemental Video 9. Upon careful observation of the active filaments, we observe the existence of three, long-lived, $+1/2$ defects as predicted in a system with $q = 3/2$. By interpolating bead-spring orientation to a director field, we can more clearly see the $+1/2$ defects and their trajectories in Figure 8b. We track these three defects over a period of simulation time and observe that their motion is consistent with the golden braid as seen in the nematohydrodynamics system with $q = 3/2$, in that the defects perform alternating swaps from each half of the cardioid. In addition, we also see the double gyre flow structure from the time-averaged vorticity of the agent-based model (Figure 8c). This double gyre structure also compares favorably to the time-averaged vorticity of the $q = 3/2$ nematohydrodynamics model shown in Figure 6b, containing alternating positive and negative values of vorticity in the upper and lower halves of the cardioid.

Unlike in the continuum nematohydrodynamics model, the agent-based model incorporates non-uniform density, where defects can be annihilated or created on the boundary between empty space and the bulk. As a result, at any given time, there may be an additional defect pair of $+1/2$ and $-1/2$ defects that quickly annihilate. However, low-density regions are a characteristic of the experimental systems of active kinesin-driven microtubules. We predict that the agent-based model, which has an active length scale and nematic coherence length that are difficult to estimate, is close to the boundary between golden braiding and metastability in Fig 7b.

IV. DISCUSSION

Our findings represent an important step in understanding the emergence and stability of ordered flows in active nematics. In particular, we have shown that by pinning defects on boundary features or by introducing extra winding into the anchoring conditions on

a disk, we both control the minimum number of motile $+1/2$ defects in the bulk and tune the active force landscape that guides the gyre structure of the time-averaged flow vorticity. Thus boundary conditions provide a way of accessing periodic, autonomous braiding dynamics of three or four $+1/2$ -defect “stirring rods” with maximal production of topological entropy. Although analogous maximal-mixing braids exist in theory for $n \geq 5 +1/2$ defects, our simulations reveal that these periodic orbits are unstable to apparently random defect motions, due to the excess of gyres over the number of $+1/2$ defects. This result suggests a general principle that matching the number of gyres to the number of $+1/2$ defects is a strategy for producing ordered flows in active nematics. This is also seen in periodic channels, where a 1D vortex lattice produces equal numbers of $+1/2$ defects and gyres, a balance that dynamically stabilizes a periodic “dance” of defects [26]. We can interpret that dance as equivalent to a silver braid, as we observed in circular confinement with $q = 4/2$ winding boundary conditions, but tiling the channel with interconnected unit cells of the braiding domain. Further, the presence of coherent flow structures in confined active nematics has been seen in channel confinement [25, 46] as well as under spatially periodic patterning of activity and external forces [14, 47].

Importantly, for the $n = 3$ and 4 defect systems, the braids found are optimally mixing for their respective number of stirring rods, supporting the notion that when not dynamically forbidden, active nematics have a spontaneous tendency to maximally mix their fluid environments [28]. While our findings do not establish spontaneous defect braiding in numbers larger than four, additional control mechanisms such as internal obstacles could potentially stabilize different braiding flow structures and defect dynamics.

Further, our results support the findings of Ref. [43] and reveal new applications for it: $\mathcal{Q} = 0$ isolines provide a subspace on which $+1/2$ defects necessarily lie. Not only are our results consistent with this rule, but this “self-constraint” interestingly requires that the defect swap events represented by braid generators are coincident with topological changes in the flow structure, in the form of reconnections in the $\mathcal{Q} = 0$ isolines.

The qualitative agreement of our agent-based model with the defect braiding and flow gyre structure predicted by our theory demonstrates the robustness of this topological approach. While the coupling between nematic order and flow takes a very different form in the agent-based model compared to Beris-Edwards nematohydrodynamics, both models support the close relationship of director topology and flow-field topology. The predictability of the vortex structure found in our work suggests that predictable dynamics from boundary-imposed active forces may be robustly observed in a broader range of confining geometries. For example, a spatially periodic tiling of obstacles can create effective active pumps [48] whose spontaneous flow structures are deducible from the

spatially periodic active forces generated at the obstacle boundaries. This principle can also create regular vortex lattices with effective anti-ferromagnetic ordering [49]. Ordered flow structures in active nematics can in turn set up ordered flows in passive liquid crystals with which they are in contact[14], which may be used to guide micro-swimmers in living liquid crystals [50].

Our findings indicate a one-to-one correspondence between the topologies of the director, the active force, and the time-averaged flow velocity field. This suggests that active force tuning is a robust driver of time averaged dynamical behavior for active nematics. Specifically, if we consider $n + 1/2$ defects in the bulk, any closed contour around them must capture a $q = n/2$ winding of the director, and thus produce an active force with a winding of $2q - 1$, as is consistent with equation 14. Further, the topology of the active force necessitates that there are $4|q - 1|$ gyres in the flow field if the average flow follows the stream lines of the active force. As all three topologies are preserved under continuous transformations, our analytic calculations for circular confinement hold for arbitrary contours. Interestingly, our prediction of $4|q - 1|$ gyres in the time-averaged flow field agrees with the findings of Ref. [23] for circular confinement with $q = 2/2$, in that experiments find circularly confined active nematics exhibit periodic switching of the handedness of the single gyre, and thus zero time-averaged vorticity.

We have demonstrated numerically that the spontaneous golden braiding of defects in cardioid confinement (Ref. [30]) are one example of a more general phenomenon, in which active nematics spontaneously adopt optimally mixing defect braiding motions if these are consistent with, and suitably constrained by, the topology

of vortices in the flow field. In confinement with circular geometry and controllable winding in the anchoring, we observed these maximally mixing periodic states in the form of the golden braid for $n = 3$ defects and the silver braid for $n = 4$. Not only are these braids consistent with those we find with tangential-anchoring boundaries with $n - 2$ cusps, but we obtained an emergent rationale for this connection through the resemblance of the latter boundaries to the envelope curves of the variable anchoring in our circular-boundary systems. Those envelopes govern defect trajectories for both periodic ($n \leq 4$) and aperiodic ($n \geq 5$) defect motions. The effective boundaries created by the envelopes, together with the gyre structures required by active forces at the boundaries, provide new principles for geometrically and topologically controlling the motions of topological defects in active nematics, potentially opening new avenues for fluid mixing applications.

ACKNOWLEDGMENTS

B.K. and D.A.B. thank Louise C. Head and Cody D. Schimming for many illuminating conversations about flow structure throughout the development of this work. A.J.S.F. thanks Jimmy Gonzalez Nuñez for his assistance in running Beris-Edwards nematohydrodynamic simulations. We thank Spencer Smith for access to the E-tec software. This material is based upon work supported by the National Science Foundation under Grant No. DMR-2225543 and the U.S. Department of Energy, Office of Science, Office of Basic Energy Sciences program under Award No. DE-SC0025803.

[1] Y. Maroudas-Sacks, L. Garion, L. Shani-Zerbib, A. Livshits, E. Braun, and K. Keren, *Nature Physics* **17**, 251 (2021).

[2] K. Copenhagen, R. Alert, N. S. Wingreen, and J. W. Shaevitz, *Nature Physics* **17**, 211 (2021).

[3] G. Duclos, C. Erlenämer, J.-F. Joanny, and P. Silberzan, *Nature Physics* **13**, 58 (2017).

[4] L. S. Hirst and G. Charras, *Nature* **544**, 164 (2017).

[5] J.-M. Armengol-Collado, L. N. Carenza, J. Eckert, D. Krommydas, and L. Giomi, *Nature Physics* **19**, 1773 (2023).

[6] B. V. Hokmabad, K. A. Baldwin, C. Krüger, C. Bahr, and C. C. Maass, *Physical Review Letters* **123**, 178003 (2019).

[7] T. Shimaya and K. A. Takeuchi, *PNAS Nexus* **1**, pgac269 (2022).

[8] A. M. Tayar, L. M. Lemma, and Z. Dogic, in *Microtubules*, Vol. 2430, edited by H. Inaba (Springer US, New York, NY, 2022) pp. 151–183, series Title: Methods in Molecular Biology.

[9] A. Doostmohammadi, J. Ignés-Mullol, J. M. Yeomans, and F. Sagués, *Nature Communications* **9**, 3246 (2018).

[10] Z. Cui, J. Su, and X. Zeng, *Current Nanoscience* **13** (2017).

[11] A. Doostmohammadi, M. F. Adamer, S. P. Thampi, and J. M. Yeomans, *Nature Communications* **7**, 10557 (2016).

[12] J. Hardöuin, R. Hughes, A. Doostmohammadi, J. Laurent, T. Lopez-Leon, J. M. Yeomans, J. Ignés-Mullol, and F. Sagués, *Communications Physics* **2**, 121 (2019).

[13] M. Serra, L. Lemma, L. Giomi, Z. Dogic, and L. Mahadevan, *Nature Physics* **19**, 1355 (2023).

[14] M. C. Calderer, L. Yao, L. Zhao, D. Golovaty, J. Ignés-Mullol, and F. Sagués, *Chevron patterns in an active nematic liquid crystal film in contact with Smectic A* (2024), arXiv:2407.01740 [cond-mat].

[15] F. L. Memarian, J. D. Lopes, F. J. Schwarzendahl, M. G. Athani, N. Sarpangala, A. Gopinathan, D. A. Beller, K. Dasbiswas, and L. S. Hirst, *Proceedings of the National Academy of Sciences* **118**, e2117107118 (2021).

[16] A. J. Tan, E. Roberts, S. A. Smith, U. A. Olvera, J. Arteaga, S. Fortini, K. A. Mitchell, and L. S. Hirst, *Nature Physics* **15**, 1033 (2019).

[17] P. W. Ellis, D. J. Pearce, Y.-W. Chang, G. Goldsztein, L. Giomi, and A. Fernandez-Nieves, *Nature Physics* **14**, 85 (2018).

[18] S. P. Thampi, R. Golestanian, and J. M. Yeomans, Phys-

ical Review E **90**, 062307 (2014).

[19] K. Thijssen, D. A. Khaladj, S. A. Aghvami, M. A. Gharbi, S. Fraden, J. M. Yeomans, L. S. Hirst, and T. N. Shendruk, Proceedings of the National Academy of Sciences **118**, e2106038118 (2021).

[20] S. Shankar and M. C. Marchetti, Physical Review X **9**, 041047 (2019).

[21] R. Zhang, S. A. Redford, P. V. Ruijgrok, N. Kumar, A. Mozaffari, S. Zemsky, A. R. Dinner, V. Vitelli, Z. Bryant, M. L. Gardel, *et al.*, Nature Materials **20**, 875 (2021).

[22] Z. Zarei, J. Berezney, A. Hensley, L. Lemma, N. Senbil, Z. Dogic, and S. Fraden, Soft Matter **19**, 6691 (2023).

[23] A. Opathalage, M. M. Norton, M. P. N. Juniper, B. Langeslay, S. A. Aghvami, S. Fraden, and Z. Dogic, Proceedings of the National Academy of Sciences **116**, 4788 (2019).

[24] M. M. Norton, A. Baskaran, A. Opathalage, B. Langeslay, S. Fraden, A. Baskaran, and M. F. Hagan, Physical Review E **97**, 012702 (2018).

[25] J. Hardoüin, C. Doré, J. Laurent, T. Lopez-Leon, J. Ignés-Mullol, and F. Sagués, Nature Communications **13**, 6675 (2022).

[26] T. N. Shendruk, A. Doostmohammadi, K. Thijssen, and J. M. Yeomans, Soft Matter **13**, 3853 (2017).

[27] C. D. Schimming, C. J. O. Reichhardt, and C. Reichhardt, Physical Review Letters **132**, 018301 (2024).

[28] K. A. Mitchell, M. M. H. Sabbir, K. Geumhan, S. A. Smith, B. Klein, and D. A. Beller, Physical Review E **109**, 014606 (2024).

[29] S. A. Smith and S. Dunn, SIAM Journal on Applied Dynamical Systems **21**, 1209 (2022).

[30] F. L. Memarian, D. Hammar, M. M. H. Sabbir, M. Elias, K. A. Mitchell, and L. S. Hirst, Physical Review Letters **132**, 228301 (2024).

[31] M. D. Finn and J.-L. Thiffeault, SIAM Review **53**, 723 (2011).

[32] A. N. Beris and B. J. Edwards, *Thermodynamics of flowing systems: with internal microstructure*, 36 (Oxford University Press, USA, 1994).

[33] L. Giomi, Physical Review X **5**, 031003 (2015).

[34] S. Ngo, A. Peshkov, I. S. Aranson, E. Bertin, F. Ginelli, and H. Chaté, Physical review letters **113**, 038302 (2014).

[35] S. J. DeCamp, G. S. Redner, A. Baskaran, M. F. Hagan, and Z. Dogic, Nature materials **14**, 1110 (2015).

[36] J.-L. Thiffeault and M. D. Finn, Philosophical Transactions of the Royal Society A: Mathematical, Physical and Engineering Sciences **364**, 3251 (2006).

[37] J.-L. Thiffeault, Physical Review Letters **94**, 084502 (2005).

[38] E. Roberts, S. Sindi, S. A. Smith, and K. A. Mitchell, Chaos: An Interdisciplinary Journal of Nonlinear Science **29** (2019).

[39] C. D. Schimming, C. Reichhardt, and C. Reichhardt, Physical Review E **108**, L012602 (2023).

[40] L. Mirantsev, The European Physical Journal E **44**, 112 (2021).

[41] C. Joshi, Z. Zarei, M. M. Norton, S. Fraden, A. Baskaran, and M. F. Hagan, Soft matter **19**, 5630 (2023).

[42] E. W. Weisstein, Epicycloid, <https://mathworld.wolfram.com/Epicycloid.html> (2003).

[43] L. C. Head, C. Dore, R. Keogh, L. Bonn, A. Doostmohammadi, K. Thijssen, T. Lopez-Leon, and T. N. Shendruk, Nature Physics **20**, 492 (2024).

[44] S. Shankar, L. V. Scharrer, M. J. Bowick, and M. C. Marchetti, Proceedings of the National Academy of Sciences **121**, e2400933121 (2024).

[45] C. D. Schimming, C. Reichhardt, and C. Reichhardt, Soft Matter **21**, 122 (2025).

[46] C. G. Wagner, M. M. Norton, J. S. Park, and P. Grover, Physical Review Letters **128**, 028003 (2022).

[47] A. Mozaffari, R. Zhang, N. Atzin, and J. J. de Pablo, Physical Review Letters **126**, 227801 (2021).

[48] I. Vélez-Ceron, R. C. Coelho, P. Guillamat, M. T. da Gama, F. Sagués, and J. Ignés-Mullol, arXiv preprint arXiv:2407.09960 (2024).

[49] C. D. Schimming, C. Reichhardt, and C. Reichhardt, Physical Review Letters **132**, 018301 (2024).

[50] T. Turiv, R. Koizumi, K. Thijssen, M. M. Genkin, H. Yu, C. Peng, Q.-H. Wei, J. M. Yeomans, I. S. Aranson, A. Doostmohammadi, *et al.*, Nature Physics **16**, 481 (2020).

[51] T. J. Chung, *Computational Fluid Dynamics* (Cambridge University Press, 2002).

[52] Code and scripts to reproduce Beris-Edwards nematodynamics data are available at B. Klein *et al.* Spontaneous-Optimal-Mixing. <https://github.com/Brandonk1/Spontaneous-Optimal-Mixing> (2025).

[53] R. Courant, E. Isaacs, and M. Rees, Communications on Pure and Applied Mathematics **5**, 243 (1952).

[54] K. P. Santo and A. V. Neimark, Advances in Colloid and Interface Science **298**, 102545 (2021).

Appendix A: Numerical methods

1. Nematohydrodynamics

a. Pressure field

In the incompressible Navier-Stokes equations 5, 6, the pressure field, p , plays the exclusive role of maintaining Eq. 6. This is achieved in our numerical implementation by taking the divergence of Eq. 5 and solving the standard pressure-Poisson scheme [51], keeping terms up to second order in derivatives of \mathbf{u} :

$$\nabla^2 p = -\nabla \cdot (\mathbf{u} \cdot \nabla) \mathbf{u} + \nabla \cdot \frac{1}{\rho} \mathbf{F} - \nabla \cdot \partial_t \mathbf{u}|_t \quad (\text{A1})$$

with a Laplacian stencil of p , such that $\nabla \cdot \partial_t \mathbf{u}|_{t+\delta t} = 0$.

We integrate equations 2 and 5 forward in time with a time step of $\delta t = 1\text{e-}4$ using the Euler method [52]. Advection terms for \mathbf{u} and Q_{ij} are calculated using an upwind scheme which computes advection coming from the direction of the local flow field [53].

b. Boundary Conditions

To simulate strong tangential anchoring on an arbitrarily curved boundary with local unit tangent $\hat{\tau}$, we apply Dirichlet conditions on $Q_{ij}|_{\partial\Omega}$:

$$\left. \begin{pmatrix} Q_{xx} \\ Q_{xy} \end{pmatrix} \right|_{\partial\Omega} (\mathbf{r}) = S \begin{pmatrix} \tau_x^2 - 1/2 \\ \tau_x \tau_y \end{pmatrix}. \quad (\text{A2})$$

In order to provide the force from such a boundary that would result in this anchoring, or equivalently that $\partial_t Q_{ij} = 0$, we set the molecular field along $\partial\Omega$ based on equation 2 as

$$H_{ij} \Big|_{\partial\Omega} = \gamma[u_k \partial_k Q_{ij} - \chi S E_{ij} + [\omega, Q] + 2\text{Tr}[QE]Q_{ij}]. \quad (\text{A3})$$

For the flow velocity field, we use a no-slip boundary condition, $\mathbf{u}|_{\partial\Omega} = 0$. Equation A1 is an instance of Poisson's equation, which has a unique solution so long as Neumann or Dirichlet boundary conditions are defined. To do this, we consider that there are no outflows or inflows along the boundary, $\hat{\nu} \cdot \mathbf{u}|_{\partial\Omega} = 0$, and derive a Neumann boundary condition using $\hat{\nu} \cdot \partial_t \mathbf{u}|_{\partial\Omega} = 0$, with $\hat{\nu}$ being the outward-pointing unit normal to the boundary and with

$$\hat{\nu} \cdot \partial_t \mathbf{u}|_{\partial\Omega} = \hat{\nu} \cdot \left[-(\mathbf{u} \cdot \nabla) \mathbf{u} + \eta \nabla^2 \mathbf{u} + \frac{1}{\rho} \mathbf{F} - \frac{1}{\rho} \nabla p \right] \Big|_{\partial\Omega}. \quad (\text{A4})$$

Upon applying the no-flux condition at the boundary, $\hat{\nu} \cdot \mathbf{u}|_{\partial\Omega} = 0$, and the corollary that the tangential derivative of the normal component of velocity must vanish, $\partial_\tau \mathbf{u} = 0|_{\partial\Omega}$, we obtain the following Neumann condition for the normal derivative of the pressure at the boundary:

$$\partial_\nu p|_{\partial\Omega} = (\rho \eta \nabla^2 u_\nu + F_\nu)|_{\partial\Omega}. \quad (\text{A5})$$

Note that $u_\nu|_{\partial\Omega} = 0$ even if there is slipping, which necessarily occurs along $\hat{\tau}$. Importantly, our scheme is generalizable to boundaries with variable curvature.

2. Agent-based model

The three-dimensional coarse-grained dynamical simulations represent active microtubules as bead-spring chain filaments, confined within a volume defined by a cardioid-shaped area with a small thickness, $L = 3.2\sigma$, in the vertical direction. Interactions between beads are represented by a short-range, repulsive, Weeks-Chandler-Anderson interaction with an additional short-range attractive depletion force:

$$U(r) = \begin{cases} 4\epsilon \left[\left(\frac{\sigma}{r} \right)^{12} - \left(\frac{\sigma}{r} \right)^6 \right] + f_{\text{dep}}r, & \text{if } r < 2^{\frac{1}{6}}\sigma, \\ 0, & \text{if } r \geq 2^{\frac{1}{6}}\sigma. \end{cases} \quad (\text{A6})$$

The bead-bead interaction has parameters of $\epsilon = 0.5$, $\sigma = 1.0$, and the additional depletion force is $f_{\text{dep}} = 0.25$. Bonded interactions between adjacent beads on each chain are represented as linear elastic springs with potential:

$$U_{\text{bond}}(r) = \frac{k_1}{2}(r - l_0)^2 \quad (\text{A7})$$

where l_0 is the equilibrium length of the spring and k_1 is the spring constant. Bond-bending terms are represented

by second- and third-neighbor linear spring interactions with spring constants k_2 and k_3 and equilibrium lengths $2l_0$ and $3l_0$:

$$U_{\text{bend}} = \frac{k_2}{2}(|\mathbf{r}_{i+2} - \mathbf{r}_i| - 2l_0)^2 + \frac{k_3}{2}(|\mathbf{r}_{i+3} - \mathbf{r}_i| - 3l_0)^2 \quad (\text{A8})$$

In Eq: A7 and Eq: A8 equilibrium length, $l_0 = 0.8$, bond spring constant, $k_1 = 57.1464$, and bend spring constants $k_2 = k_3 = 50k_1$. The equations of motion for the beads, with mass $m = 1$, are integrated using the Velocity Verlet algorithm.

Extensile activity is modeled via a pairwise active force between beads i and j on adjacent filaments with anti-polar alignment, of the form:

$$\mathbf{F}_i = \alpha \frac{\frac{1}{2}(\hat{t}_i - \hat{t}_j)}{|\mathbf{r}_{ij}|}, \quad \mathbf{F}_j = -\mathbf{F}_i, \quad (\text{A9})$$

where \hat{t} is the tangent vector of the adjacent filaments at the positions of beads i and j and activity parameter, $\alpha = 0.06$. We note that this active filament activity parameter, α , does not map to the nematohydrodynamic activity, ζ . We add a constant short-range attractive force, $\mathbf{f}_{\text{attract}}$, to the pairwise active force to represent the attractive pull of kinesin motor proteins on two adjacent filaments undergoing shear. Activity is only applied to adjacent filaments if $\hat{t}_i \cdot \hat{t}_j \leq 0.5$, resulting in extensile activity through inter-filament shear. Our coarse-grained model assumes that there is a uniform, high density, of kinesin motor proteins and adenosine triphosphate chemical energy (ATP). The model thus does not show the characteristic slowing of extensile shear as ATP density drops with time as seen in experiment [15].

To enable long-range hydrodynamic interactions, we introduce a coarse-grained two-dimensional fluid layer located below the filament volume and coupled to the filaments. This novel underlying fluid layer is introduced for two effects: to thermostat the active matter, and to provide long-range hydrodynamic interactions across areas with low active filament density. Fluid-fluid particle interactions are governed by a short-range, repulsive, Weeks-Chandler-Anderson potential similar to Eq. A6. Fluid particles are thermostatted by a pairwise dissipative particle dynamics thermostat [54]. Interactions between fluid particles and active particles are represented by a Lennard-Jones interaction with interaction strength mediated by an artificial distance offset between the fluid layer and the active layer. This interaction puts all active particles in the simulation volume in contact with the fluid thermostat.

Arbitrarily shaped boundary conditions can be imposed on both active and fluid particles in the system by generating a wall of immobile boundary particles which have an exclusively repulsive soft-sphere potential interaction. For the single-cusp cardioid system the boundary particles were laid out with the following parametric

equations:

$$\begin{aligned} x(r, \theta) &= r(1 - \cos(\theta)) \cos(\theta) \\ y(r, \theta) &= r(1 - \cos(\theta)) \sin(\theta), \end{aligned} \quad (\text{A10})$$

where $r = 123\sigma$ is the characteristic radius of the cardioid and θ is calculated to produce equally-spaced boundary particles along the perimeter of the cardioid. The spacing between boundary particles is calculated to give a uniform repulsive force along the boundary and to be small enough to effectively confine the fluid and active particles.

Appendix B: Burau Representation of \mathbf{B}_3 and \mathbf{B}_4

The Artin braid groups are closed under a product operation. The Burau representation is given by equation 9 and consists of $2(n-1)$ matrices of size $(n-1) \times (n-1)$ where the empty product and group identity is mapped to the $n-1$ dimensional identity matrix.

The elements of \mathbf{B}_3 in the Burau representation are

$$\begin{aligned} \sigma_1 &= \begin{pmatrix} 1 & 1 \\ 0 & 1 \end{pmatrix}, \quad \sigma_1^{-1} = \begin{pmatrix} 1 & -1 \\ 0 & 1 \end{pmatrix}, \\ \sigma_2 &= \begin{pmatrix} 1 & 0 \\ -1 & 1 \end{pmatrix}, \quad \sigma_2^{-1} = \begin{pmatrix} 1 & 0 \\ 1 & 1 \end{pmatrix}. \end{aligned} \quad (\text{B1})$$

An iteration of the golden braid then looks like

$$\beta_{\text{golden}} = \sigma_2^{-1} \sigma_1 = \begin{pmatrix} 1 & 0 \\ 1 & 1 \end{pmatrix} \begin{pmatrix} 1 & 1 \\ 0 & 1 \end{pmatrix} = \begin{pmatrix} 1 & 1 \\ 1 & 2 \end{pmatrix}.$$

The eigenvalues of this matrix are $\frac{3+\sqrt{5}}{2} = 1 + \phi_0 = \phi_1^2$, and $\frac{3-\sqrt{5}}{2} = 1 - (\phi_0 - 1) = (\phi_0 - 1)^2$, where $\phi_0 = \frac{1+\sqrt{5}}{2}$ is the golden ratio. Another method to see the rate of stretching is to consider the action of this braidword on an arbitrary vector $\begin{pmatrix} x \\ y \end{pmatrix}$, which gives

$$\begin{aligned} \begin{pmatrix} x' \\ y' \end{pmatrix} &= \beta_{\text{golden}} \begin{pmatrix} x \\ y \end{pmatrix} = \begin{pmatrix} 1 & 1 \\ 1 & 2 \end{pmatrix} \begin{pmatrix} x \\ y \end{pmatrix} \\ &= \begin{pmatrix} x+y \\ x+2y \end{pmatrix}. \end{aligned} \quad (\text{B2})$$

Let F_k be the k^{th} Fibonacci number. It holds that if $x = F_{n-2}$, and $y = F_{n-1}$, then

$$x' = F_{n-1} + F_{n-2} = F_n, \quad (\text{B3})$$

and

$$y' = 2F_{n-1} + F_{n-2} = F_n + F_{n-1} = F_{n+1}. \quad (\text{B4})$$

Thus, by induction, powers of β_{golden} produce the Fibonacci sequence.

The elements of \mathbf{B}_4 are given as

$$\begin{aligned} \sigma_1 &= \begin{pmatrix} 1 & 0 & 0 \\ -1 & 1 & 0 \\ 0 & 0 & 1 \end{pmatrix}, \quad \sigma_1^{-1} = \begin{pmatrix} 1 & 0 & 0 \\ 1 & 1 & 0 \\ 0 & 0 & 1 \end{pmatrix}, \\ \sigma_2 &= \begin{pmatrix} 1 & 1 & 0 \\ 0 & 1 & 0 \\ 0 & -1 & 1 \end{pmatrix}, \quad \sigma_2^{-1} = \begin{pmatrix} 1 & -1 & 0 \\ 0 & 1 & 0 \\ 0 & 1 & 1 \end{pmatrix}, \\ \sigma_3 &= \begin{pmatrix} 1 & 0 & 0 \\ 0 & 1 & 1 \\ 0 & 0 & 1 \end{pmatrix}, \quad \sigma_3^{-1} = \begin{pmatrix} 1 & 0 & 0 \\ 0 & 1 & -1 \\ 0 & 0 & 1 \end{pmatrix}. \end{aligned} \quad (\text{B5})$$

An iteration of the silver braid, $\sigma_3 \sigma_1 \sigma_2 \sigma_3^{-1} \sigma_1^{-1} \sigma_2^{-1}$, then looks like

$$\begin{aligned} \beta_{\text{silver}} &= \sigma_3 \sigma_1 \sigma_2 \sigma_3^{-1} \sigma_1^{-1} \sigma_2^{-1} \\ &= \begin{pmatrix} 1 & 0 & 0 \\ 0 & 1 & 1 \\ 0 & 0 & 1 \end{pmatrix} \begin{pmatrix} 1 & 0 & 0 \\ -1 & 1 & 0 \\ 0 & 0 & 1 \end{pmatrix} \\ &\quad \begin{pmatrix} 1 & 1 & 0 \\ 0 & 1 & 0 \\ 0 & -1 & 1 \end{pmatrix} \begin{pmatrix} 1 & 0 & 0 \\ 0 & 1 & -1 \\ 0 & 0 & 1 \end{pmatrix} \\ &\quad \begin{pmatrix} 1 & 0 & 0 \\ 1 & 1 & 0 \\ 0 & 0 & 1 \end{pmatrix} \begin{pmatrix} 1 & -1 & 0 \\ 0 & 1 & 0 \\ 0 & 1 & 1 \end{pmatrix} \\ &= \begin{pmatrix} 2 & -2 & -1 \\ -2 & 3 & 2 \\ -1 & 2 & 2 \end{pmatrix}. \end{aligned} \quad (\text{B6})$$

The eigenvalues of this matrix are $3+2\sqrt{2} = 1+2\phi_1 = \phi_1^2$, $3-2\sqrt{2} = 1-2(\phi_1-2) = (\phi_1-2)^2$, and $1 = \phi_1(\phi_1-2)$, where $\phi_1 = 1 + \sqrt{2}$ is the silver ratio. By definition both the golden and silver ratios obey the conjugate and identity relations of the metallic ratios:

$$\begin{aligned} 1 + k\phi_{k-1} &= \phi_{k-1}^2, \\ 1 - k(\phi_{k-1} - k) &= (\phi_{k-1} - k)^2, \end{aligned} \quad (\text{B7})$$

and thus,

$$\phi_{k-1}(\phi_{k-1} - k) = 1. \quad (\text{B8})$$

Appendix C: Descriptions of Supplemental Videos

Supplemental Video 1: Simulation over 3.35×10^5 time-steps of a 100×100 simulation of an active nematic confined to a disk with fixed tangential anchoring. Defect trajectories (blue and green) are shown in the disk on the left. Defect worldlines are displayed on the right. The projection axis denoted “X” is the horizontal axis of the disk.

Supplemental Video 2: (0-50 seconds) Simulation over 7.5×10^5 time-steps of a 100×100 simulation of an active nematic confined to a disk with fixed $q = 3/2$ anchoring. Defect trajectories (blue, green, and purple) are shown

in the disk on the left. Defect worldlines are displayed on the right. The projection axis denoted “X” is the horizontal axis of the disk. (50-66 seconds) Line stretching depicts an advected contour (blue) undergoing exponential stretching due to defect mixing (red). The director outside the circular domain is arbitrarily defined as horizontal and not simulated.

Supplemental Video 3: (0-33 seconds) Simulation over 5.0×10^5 time-steps of a 100×100 simulation of an active nematic confined to a disk with fixed $q=4/2$ anchoring. Defect trajectories (blue, green, and purple) are shown in the disk on the left. Defect worldlines are displayed on the right. The projection axis denoted “X” is the horizontal axis of the disk. (50-49 seconds) Line stretching depicts an advected contour (blue) undergoing exponential stretching due to defect mixing (red). The director outside the circular domain is arbitrarily defined as horizontal and not simulated.

Supplemental Video 4: Simulation over 7.5×10^5 time-steps of a 100×100 simulation of an active nematic confined to a disk with fixed $q = 3/2$ anchoring. The top three graphs show the instantaneous vorticity, the running time-averaged vorticity, and the running standard deviation of the vorticity. The bottom three graphs show the instantaneous \mathcal{Q} -criterion with $\mathcal{Q} = 0$ isolines shown in black, the running time-averaged \mathcal{Q} -criterion, and the running standard deviation of the \mathcal{Q} -criterion.

Supplemental Video 5: Simulation over 5×10^5 time-steps of a 100×100 simulation of an active nematic confined to a disk with fixed $q = 4/2$ anchoring. The top three graphs show the instantaneous vorticity, the running time-averaged vorticity, and the running standard deviation of the vorticity. The bottom three graphs show the instantaneous \mathcal{Q} -criterion with $\mathcal{Q} = 0$ isolines shown

in black, the running time-averaged \mathcal{Q} -criterion, and the running standard deviation of the \mathcal{Q} -criterion.

Supplemental Video 6: Simulation over 1.3×10^6 time-steps of a 100×100 simulation of an active nematic confined to a disk with fixed $q = 5/2$ anchoring. The top three graphs show the instantaneous vorticity, the running time-averaged vorticity, and the running standard deviation of the vorticity. The bottom three graphs show the instantaneous \mathcal{Q} -criterion with $\mathcal{Q} = 0$ isolines shown in black, the running time-averaged \mathcal{Q} -criterion, and the running standard deviation of the \mathcal{Q} -criterion.

Supplemental Video 7: Representative videos of the active phases seen in Figure 7b (left). All simulations are performed on a 200×200 lattice for 1.5×10^6 time-steps. (ℓ_a, ℓ_c) values for shown simulations are $(0.0069, 0.0625)$ for turbulent, $(0.0556, 0.0834)$ for arrested, $(0.0417, 0.0486)$ for metastable (golden), and $(0.0139, 0.0903)$ for golden braid.

Supplemental Video 8: Representative videos of the active phases seen in Figure 7b (right). All simulations are performed on a 100×100 lattice for 1.5×10^6 time-steps. (ℓ_a, ℓ_c) values for shown simulations are $(0.0131, 0.0131)$ for turbulent, $(0.0262, 0.0131)$ for arrested, $(0.0262, 0.0654)$ for metastable (silver), $(0.0196, 0.0393)$ for mixed metastable, $(0.0131, 0.1309)$ for melted, and $(0.0131, 0.1178)$ for silver braid.

Supplemental Video 9: Agent-based simulation in cardioid confinement of 64,000 active particles comprising 800 filaments, each with 80 beads, and an additional 3068 fluid particles. The left shows bead-chain filaments with green indicating CCW polar orientation and orange indicating CW polar orientation with respect to the origin. The right shows locally averaged director field and defect trajectories in blue, green, and red, performing a golden braid cycle.

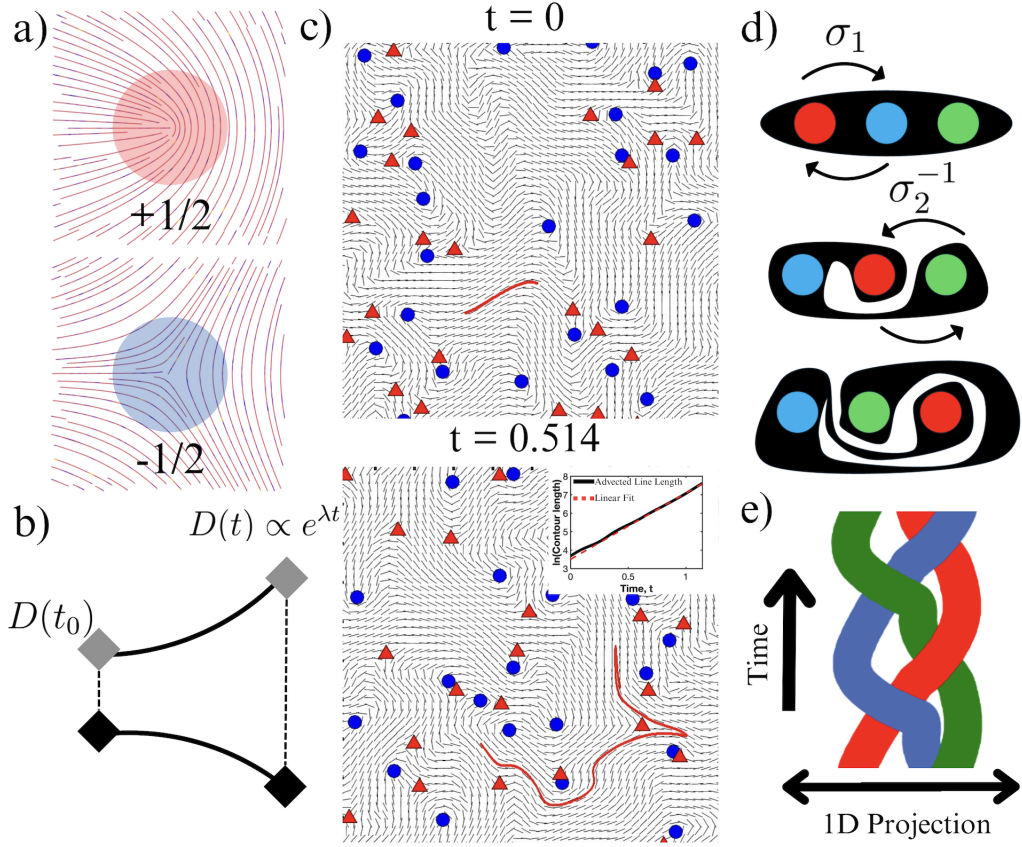


Figure 1. a) Illustrations of $\pm 1/2$ topological defects in a nematic director field. (b) Schematic illustration of the divergence of two passive tracers whose separation distance D grows exponentially in time t , giving a positive Lyapunov exponent λ . (c) Exponential stretching of a passively advected line, as a measure of topological entropy production, in simulated bulk active nematic dynamics beginning along an arbitrary contour of the director field. Inset shows the semi-log plot of the advected contour length over time. (d) Schematic mixing dynamics for ‘stirring rod’ motion described by the braid word $\{\sigma_1\sigma_2^{-1}\}$. The exponential stretching is deducible from the growth in perimeter of the black region. (e) Worldlines of topological defects for the braidword shown in (d).

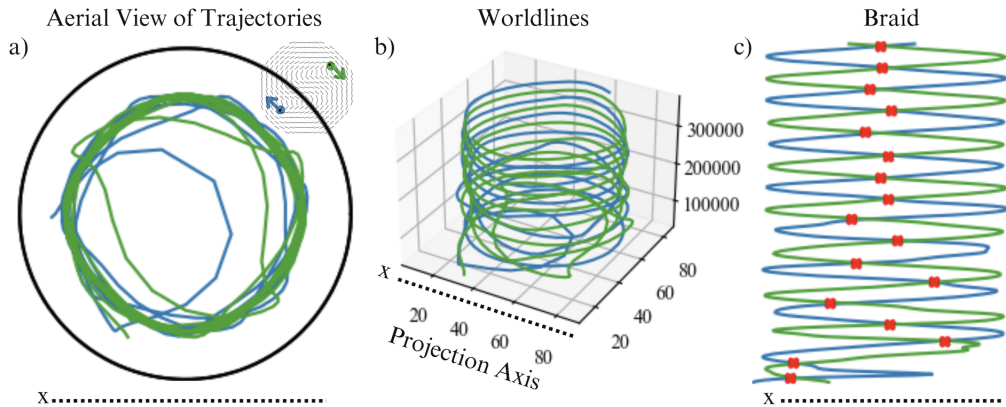


Figure 2. Braiding terminology demonstrated with two $+1/2$ defects in an active nematic confined in a circle with tangential anchoring, from a 100×100 Beris-Edwards nematic hydrodynamic simulation. (a) Trajectory traces of defects (blue and green) over simulation time (335,000 time-steps). Inset shows a snapshot of defects during cyclic motion. (b) Worldlines of the defects in (a). (c) Defect worldlines spatially projected onto the x axis. Crossings (all clockwise) are labeled by a red ‘x’; the structure is represented by the one-element braidword $\{\sigma_1\}$.

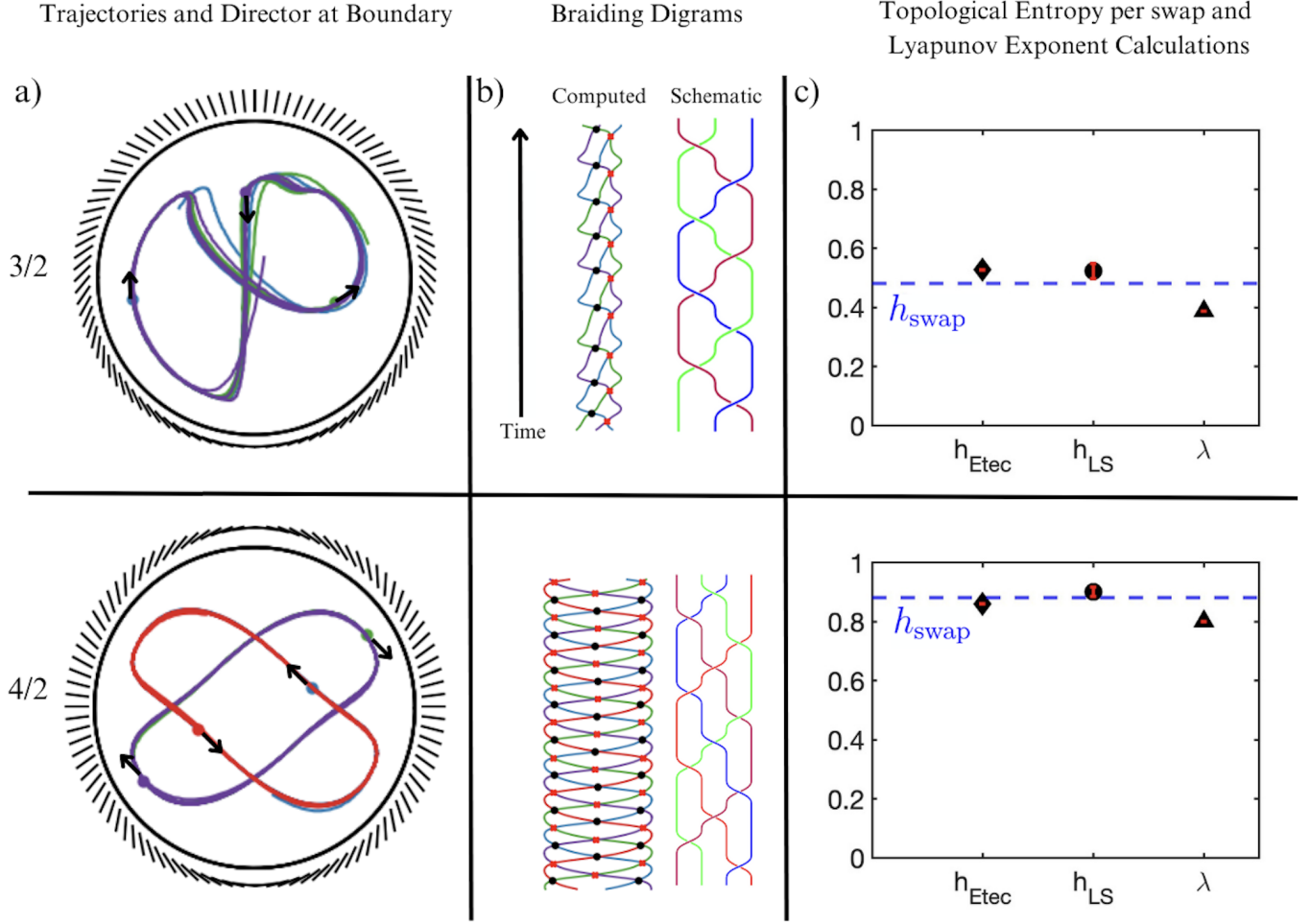


Figure 3. Periodic braiding orbits of $+1/2$ defects in a simulated active nematic confined in a disk with an anchoring direction that winds through angle $2\pi q$, for $q = 3/2$ (top row) and $q = 4/2$ (bottom row). (a) The anchoring direction along the circular boundary and defect trajectories traced over the simulation time of 7.5×10^5 ($q = 3/2$) and 5.0×10^5 ($q = 4/2$) time-steps. Each simulation was performed on a 100×100 lattice with a dimensionless active length of 0.045, and a dimensionless nematic coherence length of 0.011. Arrows indicate defect direction of motion. (b) (left) The projection of the trajectories onto the x axis, where swaps between defects are labeled with a red "x" if clockwise and a black dot if counter-clockwise; (right) schematic diagram summarizing the braid exhibited by the defects $\{\sigma_1\sigma_2^{-1}\}$ for $q = 3/2$ and $\{\sigma_1\sigma_3\sigma_2\sigma_1^{-1}\sigma_3^{-1}\sigma_2^{-1}\}$ for $q = 4/2$. (c) The numerically calculated topological entropy using the E-tec and Line Stretching (LS) algorithms (shown in Supplemental videos 2 and 3), as well as the calculated Lyapunov exponent, in units reciprocal to the time between defect swaps. Each braiding pattern consists of two effective swaps corresponding to a co-linear arrangement of defects. The numerical values of average topological entropy per swap using E-tec are 0.5277 ± 0.0005 ($q = 3/2$) and 0.8610 ± 0.0004 ($q = 4/2$) for samples of 3000 randomly initialized advected trajectories. The numerical values of average topological entropy per swap using the LS algorithm are 0.52 ± 0.03 ($q = 3/2$) and 0.90 ± 0.02 ($q = 4/2$). Errors are standard error of the mean taken over five advected curves. The numerical values of average Lyapunov exponent per swap are $0.3873 \pm .0003$ ($q = 3/2$) and $.8006 \pm .0004$ ($q = 4/2$). Each uses 350 pairs of randomly initialized passive tracers. Both of which are, as required, below their respective analytic values of topological entropy for ideal stirring rods, shown in the dashed blue line. Error bars are shown in red and are smaller than the marker size.

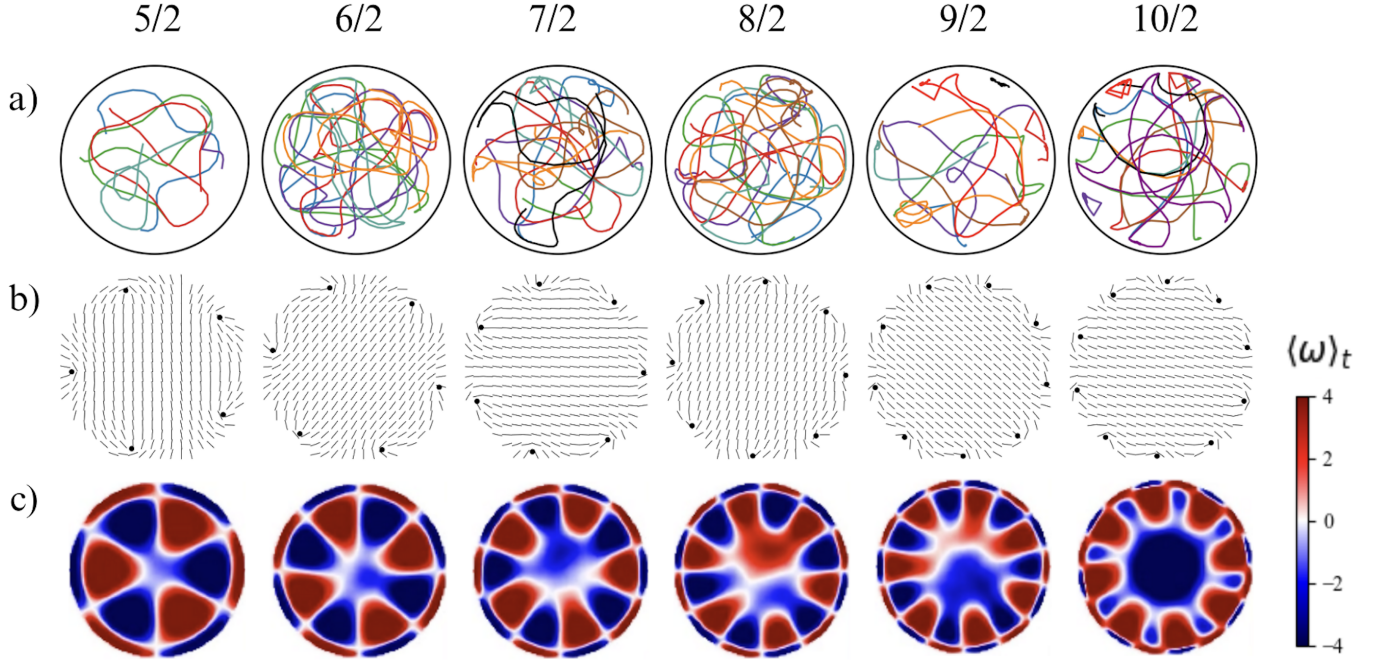


Figure 4. Defect dynamics in circular confinement with winding number $q \geq 5/2$ in the anchoring direction. Columns show the different studied values of q . a) Samples of the aperiodic trajectories. For the $q = 5/2$ system, trajectories over 40 time-steps are shown. For the $q = 6/2, 7/2, 8/2, 9/2$ systems, trajectories are shown over 100 time-steps and for $q = 10/2$ 300 time-steps are shown. b) The passive ground state configurations of the defects. In all studied geometries, the ground states show a symmetric placement of defect cores about the boundary. However, orientations of the defects are not symmetric, with orientations varying locally to match the fixed anchoring against the circular boundaries. c) The time averaged vorticity shown throughout the simulation time of 10^6 time-steps. Each simulation was performed on a 100×100 lattice, at a dimensionless active length of 0.0003, and a dimensionless nematic coherence length of 0.011.

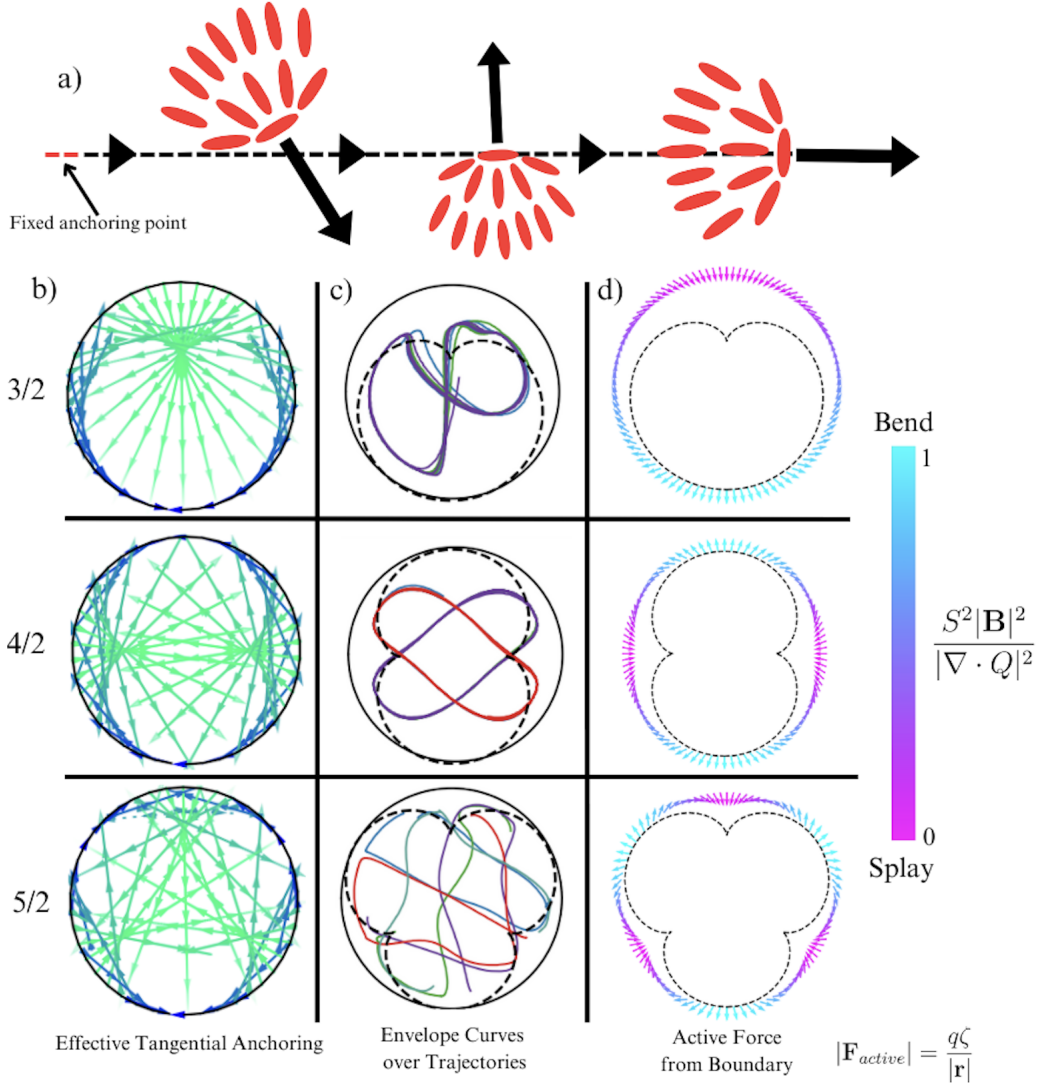


Figure 5. a) Schematic illustration of a $+1/2$ defect in three orientations and positions consistent with a line of effective tangential anchoring; arrows mark defect self-propulsion direction. The only defect orientation whose trajectory does not break an anchoring line is parallel to that line and which is away from the fixed anchoring point on the boundary. Trajectories are colored by angle with respect to \hat{r} . b) The set of lines parallel to the anchoring direction at the associated point on the surface, showing the cardioid, nephroid, and trefoiloid. (c) Envelope curves (dashed) extracted from the lines of (b), together with simulated defect trajectories. Defect trajectories tend to stay approximately within the envelopes and to intersect with the cusps in the envelope. (d) The active force (Eq. 14) imposed by the winding anchoring conditions, with splay-dominated regions in pink and bend-dominated regions in cyan. In (b)-(d), each row corresponds to the anchoring winding q labeled at left.

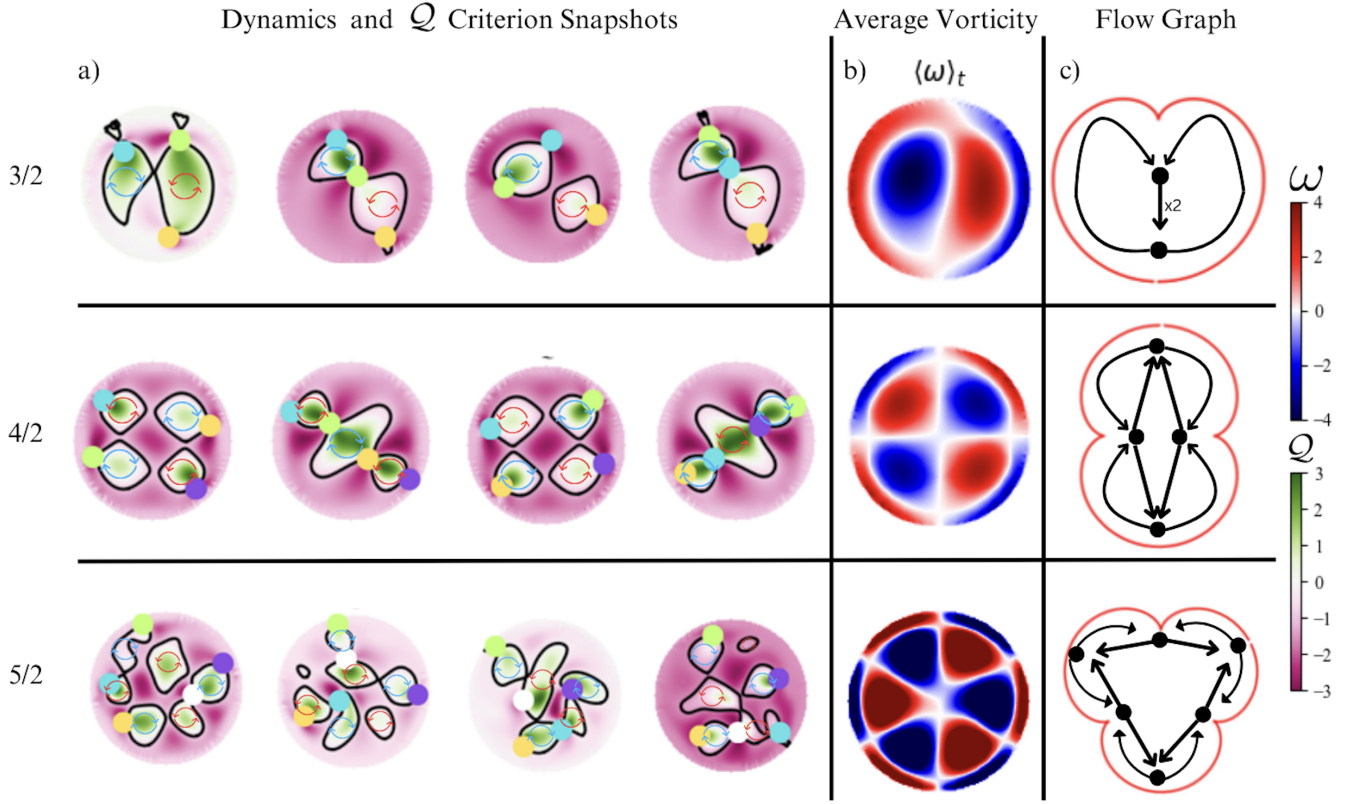


Figure 6. Coupled topologies of flow fields and topological defect trajectories in active nematics confined to disks with excess topological charge due to anchoring winding q as labeled at left. a) Snapshots from time series showing representative dynamics of $+1/2$ defects and flow fields. The magenta-green heatmaps show the Q -criterion of the flow field. Black curves are the viscometric isolines where $Q = 0$, each enclosing a vortex, whose vorticity is indicated by blue or red curved arrows. Colored circles mark the instantaneous positions of $+1/2$ defects. The braids exhibited by the $+1/2$ defects are the golden braid for $q = 3/2$ system and the silver braid for $q = 4/2$. For $q = 5/2$ (and higher) no periodic braid is observed. b) The time-averaged vorticity field, showing 2, 4, and 6 gyres for the $q = 3/2$, $4/2$, and $5/2$ systems respectively. This counting excludes the change in sign of vorticity in a narrow band near the boundary. c) Directed graphs schematically summarizing the flow structure mandated by the boundary conditions, containing $4|q - 1|$ gyres among its cycles. Each node has a total degree of 0 as is consistent with incompressible flow.

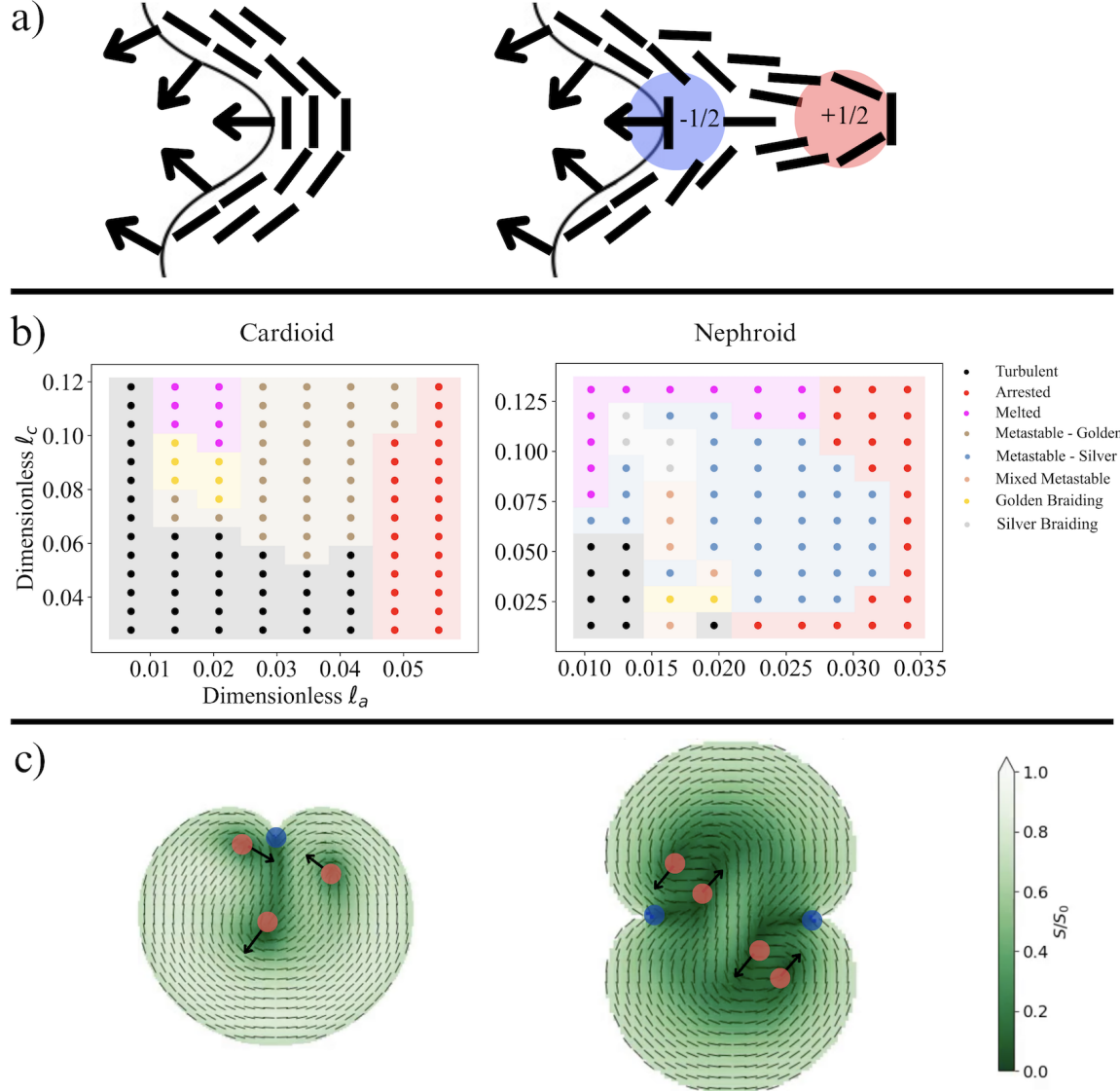


Figure 7. a) Schematic illustration of defect pinning on concave boundary features. The outwards facing normal vectors are shown as black arrows. The left image shows a non-pinning director configuration, in which there is a single bend distortion from the boundary. The right image shows defect pinning whereby the bend wall shown on the left nucleates a defect pair and pins a $-1/2$ defect against the concave boundary, and the created $+1/2$ defect moves into the nematic bulk. b) Active phase diagrams for the cardioid and nephroid epitrochoid curves using continuum Beris-Edwards nematohydrodynamics. The stability of the braiding patterns are highly dependent on the confining geometries. Cardioid simulations performed on a 200×200 lattice and nephroid simulations performed on a 100×100 lattice each for 1.5×10^6 time-steps. Simulations are labeled turbulent if there is spontaneous pair production in the nematic bulk, arrested if the defects do not move, and melted if the defect cores can not be uniquely distinguished. A braid is labeled metastable if the dynamics maintain the flow structure of the braids, but are non-pinning and/or non-cyclic, temporarily absorbing and emitting a positive defect at the cusp during the braid cycle through pair-annihilation and subsequent pair-creation of $\pm 1/2$ defects. Representative dynamics are shown in Supplemental Videos 7 and 8. c) Snapshots from braiding regimes. (ℓ_a, ℓ_c) values are $(0.0139, 0.0903)$ for the cardioid and $(0.0131, 0.1178)$ for the nephroid, showing pinned negative defects at epitrochoid cusps and motile defects in respective golden and silver braiding patterns.

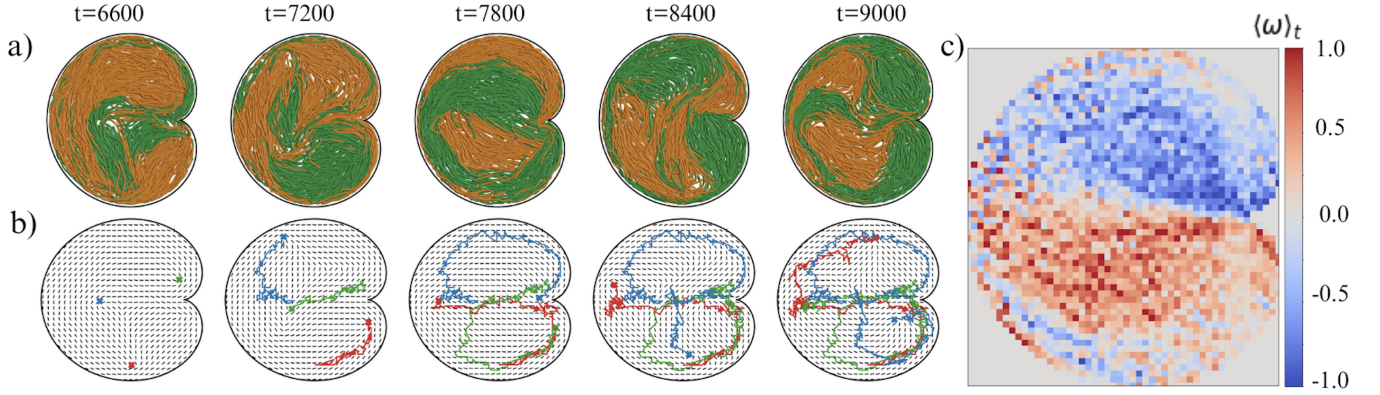


Figure 8. a) Time series of filament dynamics of the agent-based simulations of confined active nematic filaments inside the cardioid with 4×10^5 time-steps between each image shown. Green and orange indicate CCW and CW polar orientation with respect to the origin, with underlying fluid particles not visualized. Simulations consists of 800 filaments, each 80 beads long. Visualization times shown above are in arbitrary simulation time units. b) Locally-averaged director field corresponding to filament visualizations above. Three long-lived defects were tracked using the director field and their trajectories plotted over the director field showing their path and braiding dynamics. c) Time-averaged vorticity of agent-based simulations' filament particle velocities showing double gyre structure with positive vorticity shown in red and negative vorticity shown in blue. Vorticity units are $\sigma\sqrt{m/\varepsilon}$ (see Eq. A6). Full simulation with interpolated director field and extracted defect cores and trajectories is shown in Supplemental Video 9.